Article | Open Access

Energy Materials

Tan *et al. Energy Mater.* **2026**, *6*, 600119 **DOI:**10.20517/energymater.2026.166

Reversible sulfate-anion involved charge storage in layered MnO_2 for aqueous symmetric batteries

Shiyi Tan[1,#], Litao Liang[1,#], Shanshan Zhou[2], Jiaxin Meng[1], Guozhen Zhang[1], Weizhai Bao[1], Aung Ko Ko Kyaw[3], Qian Liu[2,*], Feng Yu[1,*]

Keywords:
Aqueous battery, sulfate-coupled charge compensation, layered MnO_2, symmetric cell

Citation: Tan, S.; Liang, L.; Zhou, S.; Meng, J.; Zhang, G.; Bao, W.; Kyaw, A. K. K.; Liu, Q.; Yu, F. Reversible sulfate-anion involved charge storage in layered MnO_2 for aqueous symmetric batteries. *Energy Mater.* **2026**, *6*, 600119. https://dx.doi.org/10.20517/energymater.2026.166

Received: 10 Jun 2026
First Decision: 2 Jul 2026
Revised: 1 Aug 2026
Accepted: 18 Aug 2026
Published: 16 Sep 2026

Academic Editor:
Meicheng Li
Copy Editor:
Fangling Lan
Production Editor:
Fangling Lan

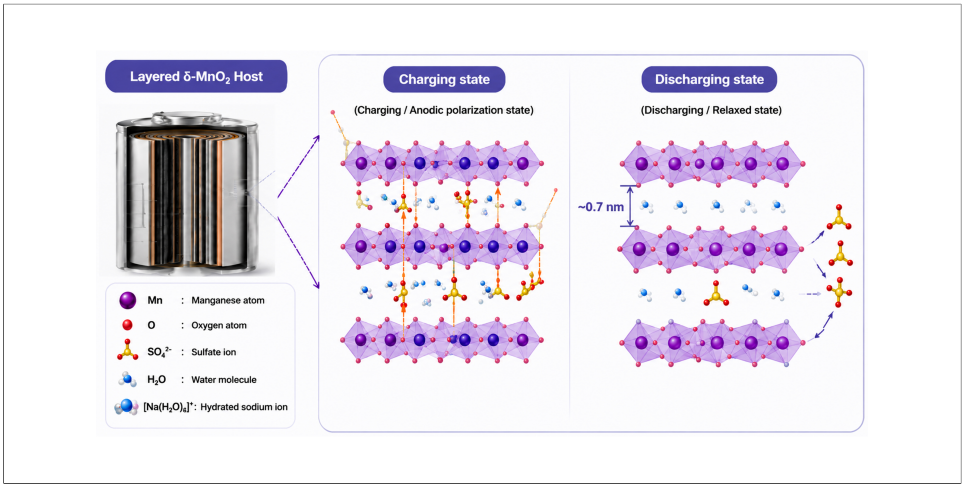

Abstract

Aqueous rechargeable batteries are promising for large-scale energy storage, but MnO_2 electrodes suffer from manganese dissolution and Jahn-Teller-related instability. Here, we investigate sulfate-anion-involved charge storage in layered δ-MnO_2 symmetric cells. *Ex situ* spectroscopy, thermal analysis, and elemental mapping show state-dependent sulfur signals accompanied by Mn valence evolution and modest, partially reversible local coordination changes. First-principles calculations indicate that sulfate accommodation and migration within a modeled interlayer are energetically plausible. These results support sulfate-coupled charge compensation and suggest possible interlayer accommodation, while surface adsorption, near-surface storage, and electrolyte trapping cannot be excluded under the present *ex situ* conditions. The MnO_2 electrode delivers 154.2 mAh g^{-1}

[1]Jiangsu Key Laboratory of New Energy Devices & Interface Science, School of Chemistry and Materials Science, Nanjing University of Information Science and Technology, Nanjing 210044, Jiangsu, China.
[2]Centre for Materials Science, School of Chemistry and Physics, Faculty of Science, Queensland University of Technology, Brisbane, QLD 4001, Australia.
[3]Department of Electronic and Electrical Engineering, Southern University of Science and Technology, Shenzhen 518055 Guangdong, China.
[#]Authors contributed equally.

***Correspondence to:** Dr. Qian Liu, Centre for Materials Science, School of Chemistry and Physics, Faculty of Science, Queensland University of Technology, Brisbane, QLD 4001, Australia. E-mail: q30.liu@qut.edu.au; Dr. Feng Yu, Jiangsu Key Laboratory of New Energy Devices & Interface Science, School of Chemistry and Materials Science, Nanjing University of Information Science and Technology, Nanjing 210044, Jiangsu, China. E-mail: yufeng@nuist.edu.cn

at 0.2 A g^{-1}, and the symmetric cell achieves 107.94 Wh kg^{-1} at 180 W kg^{-1} with 93.7% capacity retention after 3,000 cycles. This work provides evidence for sulfate-coupled charge compensation in layered MnO_2.

INTRODUCTION

Aqueous rechargeable batteries have attracted considerable attention as candidates for large-scale energy storage because of their low cost, high safety, environmental compatibility, and high ionic conductivity[1-3]. Compared with conventional organic-electrolyte batteries, aqueous systems provide a safer and more sustainable platform for large-scale energy storage[4-6]. Developing high-performance aqueous batteries with stable electrode materials and efficient charge-storage mechanisms is therefore an important research focus[7-9]. Recent advances in transition-metal-based electrode materials have further demonstrated that rational regulation of crystal structure, accessible redox sites, ion-transport pathways, and electrode-electrolyte interfaces is essential for balancing capacity, reaction kinetics, and cycling durability[10-14]. Among candidate materials, manganese dioxide (MnO_2) has been widely studied because of its high theoretical capacity (308 mAh g^{-1}), natural abundance, low toxicity, and environmental compatibility[15,16]. Layered δ-MnO_2 is particularly attractive due to its two-dimensional framework of edge-sharing [MnO_6] octahedra, with interlayer spacing of approximately 0.7 nm, which provides accessible galleries for electrolyte penetration, ion transport, and possible ion accommodation[13,17]. This open layered structure makes δ-MnO_2 a suitable platform for investigating both intercalation-type and surface- or near-surface charge-storage processes. It is also attractive for aqueous symmetric cells, in which the same electrode material can be employed at both sides, thereby simplifying material selection and cell fabrication[18-20].

Despite these advantages, MnO_2 electrodes often suffer from limited rate capability and cycling stability. Accumulation of Mn^{3+} can induce Jahn-Teller distortion of the MnO_6 octahedra, causing local structural deformation and degradation of the layered framework[21,22]. In addition, manganese dissolution in aqueous electrolytes can accelerate capacity decay. Sluggish ion transport, irreversible phase evolution, and lattice strain may further contribute to electrochemical degradation. These challenges motivate the exploration of alternative charge-storage pathways and material-design strategies that maintain electrochemical reversibility while minimizing irreversible structural and chemical evolution[22,23].

Conventional MnO_2 aqueous batteries typically rely on metallic cation carriers such as Li^+, Na^+, K^+, Zn^{2+}, and Al^{3+}[24]. While these cations enable charge compensation through insertion or adsorption, their transport kinetics and structural effects depend strongly on ionic size, charge density, hydration environment, and the geometry of the host structure. Desolvation and solid-state diffusion may limit reaction kinetics, whereas repeated lattice insertion and extraction can induce local strain or irreversible structural rearrangement[25]. Non-metallic charge carriers, particularly inorganic anions, may provide alternative charge-compensation pathways that differ from conventional cation-dominated storage[26,27]. Among these, sulfate anions (SO_4^{2-}) are inexpensive, environmentally benign, and widely available. In sulfate-containing aqueous electrolytes, SO_4^{2-} may participate in electrochemical charge compensation through interfacial adsorption, surface or near-surface storage, and, in structurally suitable hosts, possible interlayer accommodation[28,29]. Nevertheless, because SO_4^{2-} is a relatively large and strongly hydrated divalent anion, its electrochemical participation is expected to depend strongly on host geometry, solvation effects, and the applied electrode potential.

The layered δ-MnO_2 structure provides a potential framework for sulfate-anion storage[30-32]. During electrochemical polarization, reversible uptake of sulfate-containing species into or onto the MnO_2 electrode may contribute to charge compensation associated with Mn valence evolution[33]. Such anion-involved charge compensation would differ from a purely metallic-cation-dominated mechanism and could alter the interfacial and bulk redox chemistry of the electrode[34-36]. Compared with layered δ-MnO_2, tunnel- and

rutile-type MnO_2 structures generally provide more spatially confined ion-transport pathways and may therefore impose greater steric and desolvation constraints on the accommodation of bulky sulfate anions[37-39].

In this work, layered δ-MnO_2 was synthesized via a hydrothermal method and investigated to clarify sulfate-anion-involved charge storage in aqueous electrolytes and symmetric cells. Structural characterization confirmed its layered framework and nanosheet-assembled morphology. *Ex situ* X-ray photoelectron spectroscopy (XPS) and X-ray absorption spectroscopy (XAS) reveal reversible Mn valence evolution during electrochemical polarization, whereas thermogravimetric analysis (TGA) and elemental mapping show an increased amount of sulfur-containing species in the charged electrode and a pronounced decrease after discharge. First-principles calculations further indicate that sulfate migration within the interlayer region of δ-MnO_2 is energetically feasible, with a calculated migration barrier of approximately 0.22 eV. Taken together, these observations support reversible sulfate participation in the charge-storage process and indicate that interlayer accommodation is energetically plausible. However, the present *ex situ* measurements do not uniquely establish the location of sulfate-containing species, and surface adsorption, near-surface storage, and electrolyte trapping remain possible contributions. Electrochemical testing shows a specific capacity of 154.2 mAh g^{-1} at 0.2 A g^{-1}. The assembled MnO_2//MnO_2 symmetric cell delivers an energy density of 107.94 Wh kg^{-1} at a power density of 180 W kg^{-1} and 55.8 Wh kg^{-1} at a power density of 900 W kg^{-1} while retaining 93.7% of its initial capacity after 3,000 cycles. These findings provide evidence for sulfate-coupled charge compensation in layered MnO_2 and establish a basis for further operando and quantitative investigations of anion-involved charge storage in aqueous manganese-based batteries.

EXPERIMENTAL

Materials synthesis of layered δ-MnO_2

Layered δ-MnO_2 was prepared using a modified single-step hydrothermal route. Briefly, 2.0 g of manganese sulfate monohydrate ($MnSO_4·H_2O$) and 4.0 g of ammonium persulfate ($(NH_4)_2S_2O_8$) were introduced sequentially into 80 mL of deionized water. The mixture was magnetically stirred vigorously at room temperature for 30 min, yielding a clear and homogeneous pale-pink precursor solution. This treatment promoted the uniform dispersion of Mn^{2+} and $S_2O_8^{2-}$ species in the solution.

The resulting precursor solution was loaded into a 100 mL Teflon-lined stainless-steel autoclave, sealed, and subsequently heated in a thermostatically controlled oven. The autoclave was heated from ambient temperature to 140 °C at approximately 5 °C min^{-1} and held at this temperature for 12 h. Under these hydrothermal conditions, decomposition of $S_2O_8^{2-}$ generated oxidizing species that facilitated the oxidation of Mn^{2+} and the subsequent formation of layered MnO_2.

Once the reaction mixture had cooled naturally to room temperature, the resulting black precipitate was isolated by centrifugation at 8,000 rpm for 5 min. The recovered solid was subjected to three washing cycles with deionized water, and ultrasonication was performed during each cycle to facilitate the removal of residual soluble species. This was followed by three additional washing cycles with absolute ethanol to displace surface-bound water and promote subsequent drying. The washed product was subsequently vacuum-dried at 60 °C for 12 h. After drying, the black solid was gently pulverized using an agate mortar to obtain a homogeneous fine powder. The resulting powder was kept in a sealed desiccator until further use.

Electrode preparation

For electrode preparation, the as-prepared δ-MnO_2 powder was blended with acetylene black to improve the electrical conductivity of the electrode. A diluted polytetrafluoroethylene (PTFE) emulsion with a solid content of approximately 10 wt% was subsequently introduced dropwise during continuous stirring or

grinding, promoting PTFE fibrillation and the formation of a cohesive, dough-like paste. The resulting paste was rolled into a thin, uniform film and then mechanically pressed onto precleaned titanium foil serving as the current collector. Before electrochemical testing, the fabricated electrodes were vacuum-dried to remove residual solvent and moisture.

Materials characterizations

The structural, morphological, and surface chemical properties of the prepared samples were examined using the following analytical techniques. Powder X-ray diffraction (XRD) patterns were recorded using a SmartLab diffractometer (Rigaku, Japan) equipped with a Cu Kα radiation source (λ = 1.54059 Å). Data were collected over a 2θ range of 5°-90° at a scanning rate of 5° min^{-1}. Scanning electron microscopy (SEM) imaging and elemental mapping were carried out on a GeminiSEM 300 microscope (Zeiss), operated at accelerating voltages of 5-15 kV. Surface chemical states were analyzed by XPS using an ESCALAB 250Xi system (Thermo Fisher Scientific, USA) equipped with a monochromated Al Kα source. The binding-energy scale of each spectrum was referenced to the C 1s peak. Mn K-edge XAS data were acquired at beamline 12-ID of the Australian Synchrotron, operated by ANSTO, Australia, using a Si(111) double-crystal monochromator.

Electrochemical measurements

Electrochemical performance was evaluated using both a three-electrode setup and a two-electrode symmetric-cell configuration. Three-electrode measurements were conducted in a 50 mL Luggin-type electrochemical cell. The as-prepared MnO_2 electrode, a platinum sheet, and a saturated calomel electrode (SCE) were employed as the working, counter, and reference electrodes, respectively. An aqueous solution of 0.5 M $(NH_4)_2SO_4$ served as the electrolyte. Cyclic voltammetry (CV) and galvanostatic charge-discharge (GCD) tests were conducted over a potential range of 0-1.2 V *vs.* SCE. CV curves were recorded at scan rates of 1-5 mV s^{-1} to examine the redox response and charge-storage kinetics of the MnO_2 electrode. GCD profiles were collected at current densities ranging from 0.2 to 1.0 A g^{-1} for determination of the specific capacity and rate capability.

For the aqueous symmetric cell, two nominally identical MnO_2 electrodes were employed at the positive and negative sides. The MnO_2//MnO_2 device was assembled with 0.5 M aqueous Na_2SO_4 as the electrolyte, CV measurements were performed over progressively expanded cell-voltage windows from −0.5 to +0.5 V to −2.0 to +2.0 V. GCD measurements at different current densities were used to determine the specific capacity, rate capability, energy density, and power density of the device. Long-term durability was assessed through continuous galvanostatic cycling, with the Coulombic efficiency for each cycle calculated as the ratio of discharge capacity to charge capacity.

CV and other three-electrode measurements were performed using a CHI 660E/760E electrochemical workstation, whereas GCD and prolonged cycling tests were conducted on a BTS-4008 battery testing system (Neware, China). Unless otherwise stated, the specific capacity, specific capacitance, energy density, and power density were based on the active MnO_2 mass of working (single) electrode.

RESULTS AND DISCUSSION

Layered MnO_2 was synthesized using the hydrothermal procedure described in the Experimental section. The morphology and crystal structure of the as-prepared sample were first characterized by SEM, transmission electron microscopy (TEM), selected-area electron diffraction (SAED), and XRD. As shown in Figure 1A, the SEM image reveals that the product consists of micrometer-scale secondary aggregates assembled from nanosheet subunits. The TEM image in Figure 1B provides local nanoscale structural information and reveals thin nanosheet subunits. The SAED pattern in Figure 1C exhibits diffuse diffraction

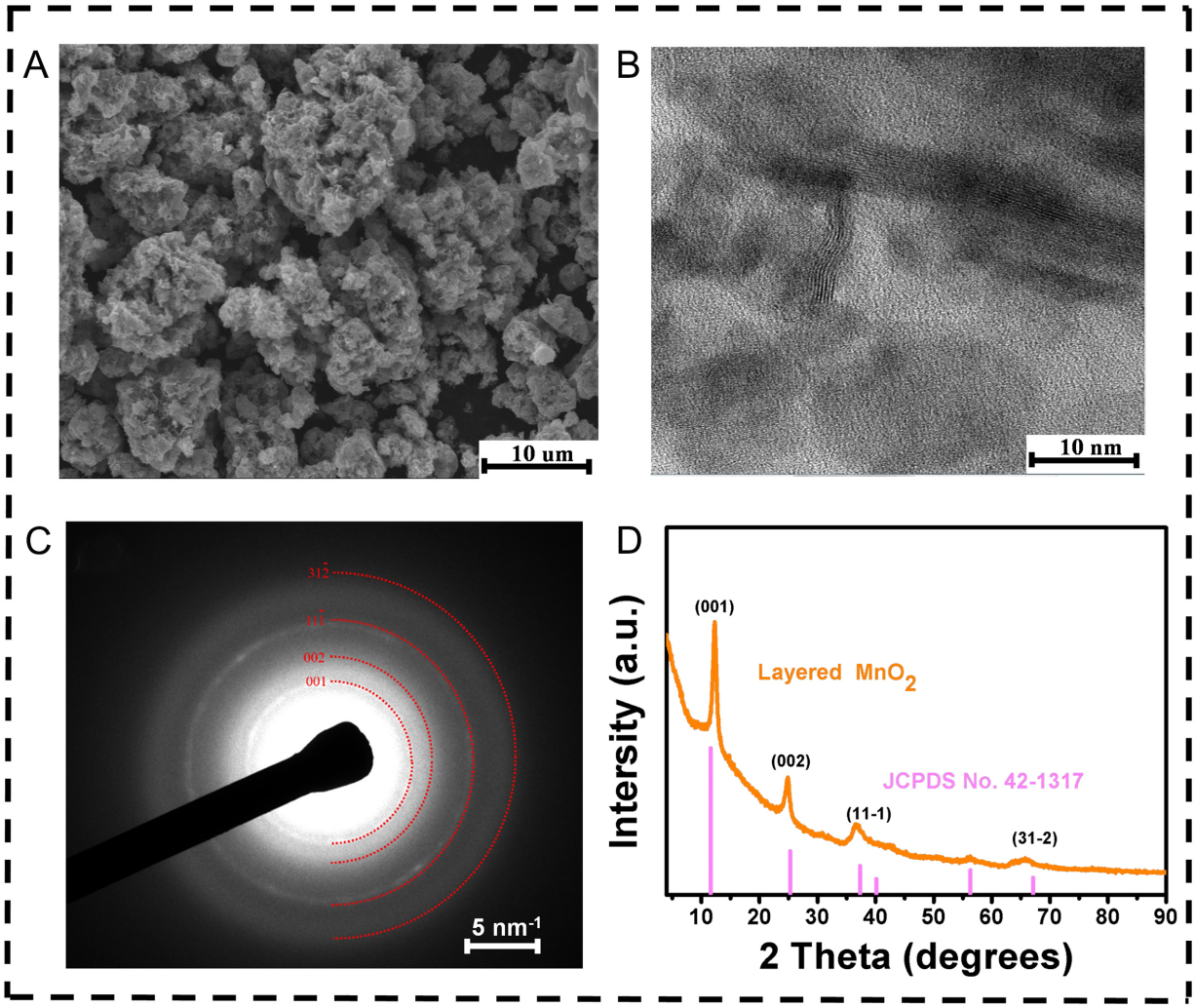

Figure 1. Structural and spectroscopic characterizations of layered MnO_2. (A) SEM image, (B) TEM image, and (C) SAED image of the as-prepared layered MnO_2. (D) Powder XRD pattern of the layered MnO_2 powder.

rings, supporting the presence of nanosized crystalline domains with limited long-range ordering. The measured lattice spacing [Supplementary Figure 1] is approximately 0.7 nm, which is consistent with the interlayer spacing of layered δ-MnO_2. This relatively open interlayer gallery provides geometrical space for electrolyte access and possible ion accommodation.

The crystal structure of the layered MnO_2 was further confirmed by XRD. As shown in Figure 1D, the diffraction peaks located at 12.6°, 25.3°, 37.3°, and 65.5° can be indexed to the (001), (002), (11-1), and (31-2) planes of layered δ-MnO_2, respectively, consistent with the reference pattern of δ-MnO_2 (PDF No. 42-1317)[40]. The estimated lattice parameters are a = 5.15 Å, b = 2.84 Å, and c = 7.16 Å, which are consistent with a layered δ-MnO_2 phase. The broad diffraction features indicate a small coherent domain size and limited long-range structural ordering, consistent with the nanosheet morphology observed by TEM and the diffuse diffraction rings in the SAED pattern.

The textural properties of the layered MnO_2 were evaluated using N_2 adsorption-desorption measurements, as shown in Figure 2A and B. The Brunauer-Emmett-Teller (BET) specific surface area was determined to be 75.3 $m^2 g^{-1}$, and the observed pore-size distribution is attributed predominantly to interparticle voids formed between the nanosheet-assembled secondary particles. Such porous features may facilitate electrolyte

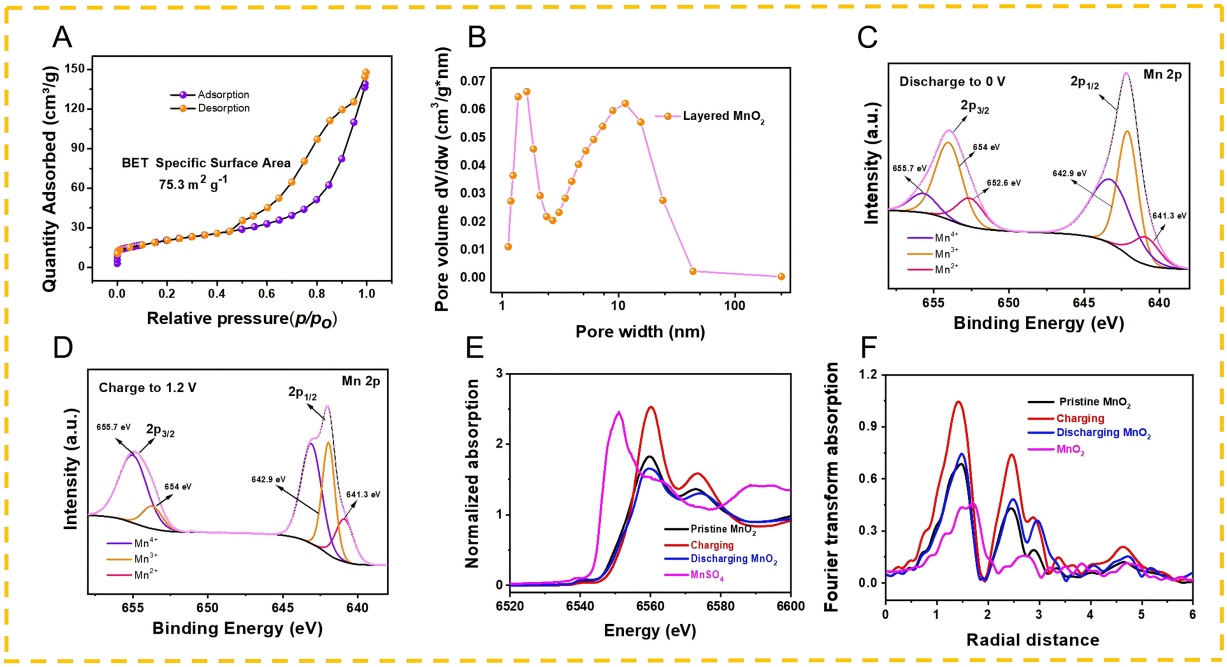

Figure 2. Textural and spectroscopic characterization of layered MnO_2 electrodes. (A) N_2 adsorption-desorption isotherm and (B) pore-size distribution of layered MnO_2. *Ex situ* Mn 2p XPS spectra of MnO_2 electrodes at (C) discharged state of 0 V and (D) charged state of 1.2 V. *Ex situ* Mn K-edge XANES (E) and Fourier-transform EXAFS (F) spectra at different charge/discharge states.

penetration and shorten transport distances within the electrode, thereby providing accessible electrode-electrolyte interfaces during electrochemical operation. It should be noted that the BET surface area and pore-size distribution mainly reflect the accessible surface and interparticle porosity of the material; therefore, they are discussed here as structural characteristics favorable for electrolyte accessibility rather than as direct proof of sulfate-anion intercalation.

To investigate Mn valence evolution during electrochemical operation, *ex situ* XPS measurements were performed on MnO_2 electrodes collected at selected electrochemical states. The Mn 2p XPS spectra provide surface-sensitive information regarding the surface oxidation states of Mn. As shown in Figure 2C and D, the Mn 2p spectra exhibit two main spin-orbit components centered at approximately 642.5 and 654.0 eV, which can be assigned to Mn $2p_{3/2}$ and Mn $2p_{1/2}$, respectively. Peak deconvolution suggests contributions from Mn species with different oxidation states, consistent with the mixed-valence character commonly reported for birnessite-type and layered MnO_2 materials[41]. Because Mn 2p spectra exhibit substantial multiplet splitting, satellite features, and overlap among different oxidation states, the fitted components are interpreted qualitatively rather than as an absolute quantification of Mn^{2+}, Mn^{3+}, and Mn^{4+} contents. Based on the fitting model and literature assignments, the lower-binding-energy contributions were tentatively associated with relatively reduced Mn species, whereas the higher-binding-energy contributions were assigned to more oxidized Mn species. The detailed fitting parameters and assignment criteria are provided in the Supplementary Materials. At the discharged state of 0 V, the Mn 2p spectrum contains a relatively higher contribution of low-valence Mn species. After charging to 1.2 V, the relative intensity of the lower-binding-energy contribution decreases, while the higher-binding-energy contribution becomes more pronounced, indicating a shift toward a more oxidized surface Mn state during the charging process. Similar reversible Mn valence modulation has been reported in aqueous MnO_2-based electrodes during electrochemical charge/discharge processes[42]. The observed spectral evolution indicates that Mn-centered redox reactions contribute to electrochemical charge compensation. When considered together with the state-dependent changes in sulfur-containing species discussed below, these results are consistent with sulfate participation in

the overall charge-storage process.

To further probe the electronic structure and local coordination environment of Mn during electrochemical polarization in the sulfate-containing electrolyte, XAS measurements were performed. The Mn K-edge XANES spectra [Figure 2E] show an apparent shift of the absorption edge to higher energy after charging to 1.2 V relative to the pristine electrode, while the $MnSO_4$ spectrum serves as a low-valence Mn^{2+} reference, indicating an increase in the average Mn oxidation state during electrochemical polarization. Such edge-position variation is commonly associated with Mn valence evolution in aqueous MnO_2-based electrodes, as reported in previous XAS studies of manganese oxide battery systems[43]. The variation in the main absorption feature after charging further indicates a change in the Mn electronic and local coordination environment[44]. Notably, the overall XANES profile of the pristine electrode lies between those of the charged and discharged states, further indicating a state-dependent evolution of the Mn electronic structure during electrochemical polarization.

Fourier-transformed EXAFS spectra [Figure 2F] reveal two dominant scattering features at approximately 1.5 and 2.3 Å without phase correction, which can be assigned to the first-shell Mn-O scattering path and the higher-shell Mn-Mn scattering contribution in edge-sharing MnO_6 octahedra, respectively. During charging, the Mn-O peak intensity increases slightly, indicating a modest change in the local Mn-O coordination environment. The Mn-Mn correlation peak exhibits only minor intensity variation, suggesting that no pronounced loss of the short-range Mn-Mn correlation occurs at the examined charged state. It should be emphasized that EXAFS peak amplitudes are influenced by coordination number, structural disorder, the Debye-Waller factor, and data-processing parameters. In the absence of quantitative EXAFS fitting, changes in peak intensity cannot be uniquely attributed to increased local symmetry, suppression of Jahn-Teller distortion, or preservation of the complete layered framework. Upon discharge, both Mn-O and Mn-Mn features shift in intensity toward those of the initial state, suggesting that at least part of the local coordination response is reversible. The subtle changes in EXAFS features are therefore consistent with modest and partially reversible short-range coordination changes during electrochemical cycling; however, they do not independently identify the charge-compensating ionic species or exclude longer-range structural degradation. Overall, the combined XANES and EXAFS analyses support reversible Mn-centered redox activity accompanied by modest changes in the local coordination environment of layered MnO_2. The XAS results do not, by themselves, establish the origin of the pseudocapacitive response. The kinetic characteristics of the charge-storage process are evaluated separately using scan-rate-dependent electrochemical analysis, whereas the present spectroscopic results provide complementary evidence for Mn redox and a comparatively limited short-range structural response under the examined *ex situ* conditions.

To evaluate the possible uptake of sulfate-containing species in layered MnO_2, *ex situ* TGA was carried out on electrodes collected after charging to 1.2 V and discharging to 0 V *vs.* SCE. As shown in Figure 3A, the charged MnO_2 electrode exhibits a larger overall mass loss than the discharged electrode, indicating a greater amount of thermally removable or decomposable species in the charged sample. The difference in mass loss between the charged and discharged electrodes is approximately 20.2 wt%. Because the additional mass loss may contain contributions from sulfate-containing species, residual electrolyte, adsorbed or structural water, and other electrode components, the 20.2 wt% difference is regarded as a semi-quantitative estimate rather than a definitive sulfate content. When interpreted together with the state-dependent sulfur signals obtained from elemental and spectroscopic analyses, the TGA results support the electrochemically associated uptake and subsequent removal of sulfur-containing species. Nevertheless, these *ex situ* measurements do not independently distinguish interlayer sulfate accommodation from surface adsorption, near-surface association, or residual electrolyte retained within the porous electrode.

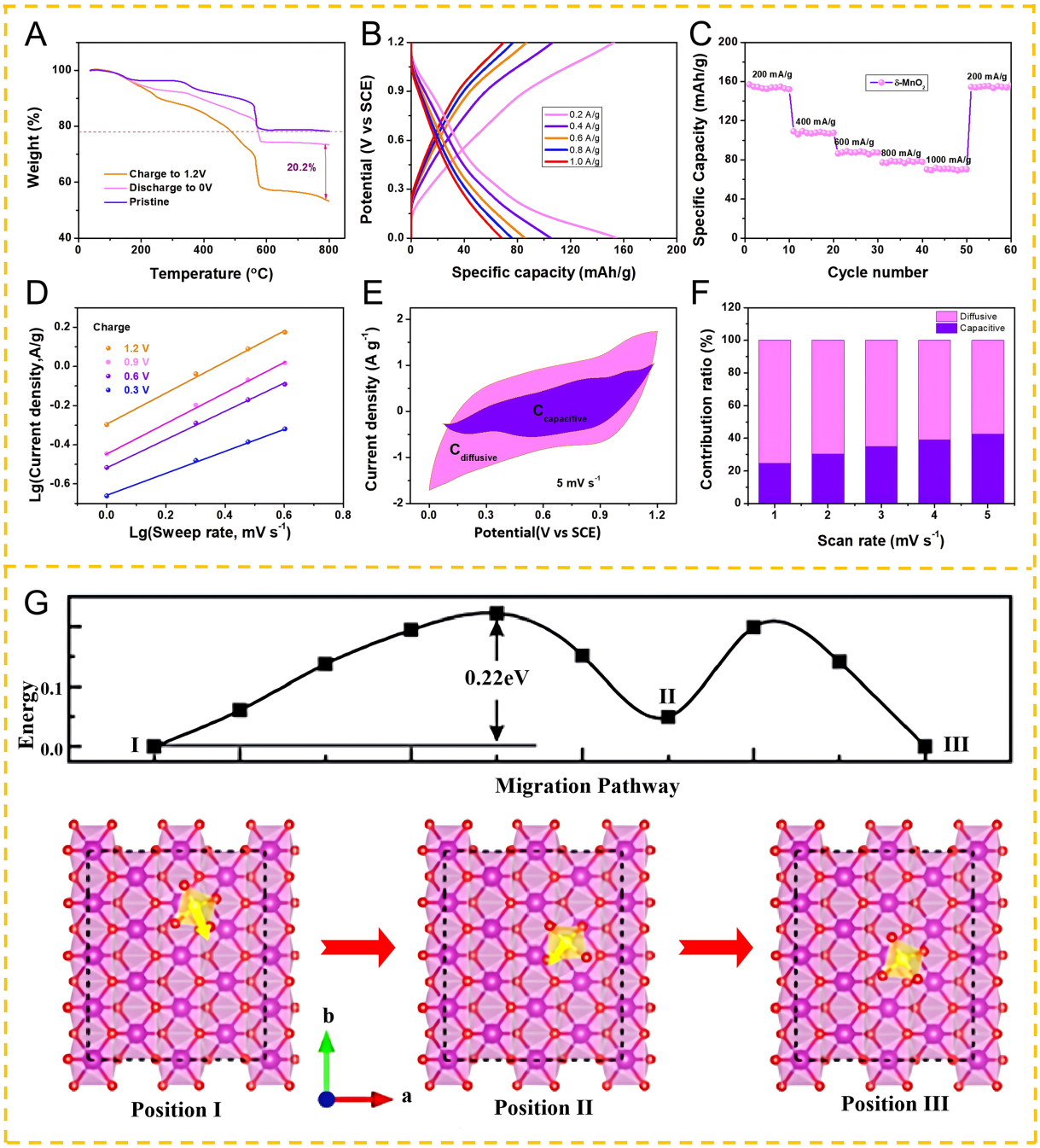

Figure 3. Electrochemical and thermal characterization of layered MnO_2 electrodes. (A) *Ex situ* TGA curves of pristine, charged, and discharged electrodes under argon atmosphere. (B) Typical galvanostatic charge-discharge (GCD) profiles of the layered MnO_2 electrode. (C) Rate performance of the layered MnO_2 electrode at various current densities. (D) Log(i) *vs.* log(v) plot for the layered MnO_2 electrode, illustrating the *b*-value analysis of charge-storage kinetics. (E) Non-diffusion-controlled (capacitive) current contribution at a scan rate of 5 mV s^{-1}. (F) Histogram showing the capacitive contribution at scan rates from 1 to 5 mV s^{-1}. (G) Calculated migration pathway and energy barrier of SO_4^{2-} within the modeled MnO_2 interlayer environment.

The electrochemical behavior of the layered MnO_2 electrode was investigated in a three-electrode configuration over a potential window of 0-1.2 V *vs.* SCE. Figure 3B shows the GCD profiles at current densities ranging from 0.2 to 1.0 A g^{-1}. The curves exhibit nearly symmetric and continuously sloping profiles without an obvious voltage plateau, which is consistent with a broad distribution of redox potentials and the absence of a sharply defined two-phase reaction. The rate performance is summarized in Figure 3C. The

layered MnO_2 electrode delivers specific capacities of 154.2, 106.0, 88.5, 76.6, and 70.8 mAh g^{-1} at current densities of 0.2, 0.4, 0.6, 0.8, and 1.0 A g^{-1}, respectively. Although the capacity gradually decreases with increasing current density, it recovers to approximately 154.2 mAh g^{-1} when the current density returns to 0.2 A g^{-1}, indicating that most of the initial low-rate capacity is recovered after operation at higher current densities. The capacity decay at higher current densities may arise from increased electrochemical polarization, shorter reaction times, and kinetic limitations that restrict the utilization of electrochemically accessible regions under rapid charge-discharge conditions.

To further evaluate the electrochemical response and kinetic characteristics of the layered MnO_2 electrode, CV measurements were conducted at different scan rates from 1 to 5 mV s^{-1}, as shown in Supplementary Figure 2. The CV curves exhibit quasi-rectangular profiles with broad redox features, indicating that the charge-storage response contains Faradaic redox contributions superimposed on a capacitive-like background. With increasing scan rate, the overall shape of the CV curves is largely maintained, although moderate peak broadening and potential shifts may arise from increased electrochemical polarization. The retention of the overall curve shape over the examined scan-rate range suggests that the principal electrochemical reactions remain similar, but it does not by itself establish rapid ion transport or complete electrochemical reversibility. Based on these CV curves, the relationship between peak current and scan rate was further analyzed to assess the relative influence of capacitive-controlled and diffusion-influenced kinetics.

The relationship between peak current and scan rate can be expressed by:

$$i = av^b \tag{1}$$

where i is the peak current, v is the scan rate, and a and b are adjustable parameters.

Generally, a b value close to 0.5 indicates a diffusion-controlled process, whereas a b value close to 1.0 suggests capacitive-controlled behavior. As shown in Figure 3D, the calculated b values at four representative (0.3, 0.6, 0.9, 1.2 V *vs.* SCE) potentials are 0.56, 0.69, 0.75, and 0.76, respectively. These intermediate values indicate a mixed kinetic response involving both diffusion-influenced and capacitive-controlled processes. The relatively lower (b) value of 0.56 suggests a stronger diffusion influence at the corresponding potential, whereas the values of 0.69-0.76 indicate a comparatively larger capacitive-controlled contribution at the other selected potentials.

The capacitive contribution was further quantified at different scan rates. As shown in Figure 3E and F, the capacitive contribution increases from 24.7% to 42.5% as the scan rate increases from 1 to 5 mV s^{-1}. This trend indicates that rapidly responding charge-storage processes become increasingly important at higher scan rates, whereas the diffusion-influenced contribution decreases from 75.3% to 57.5% but remains the larger component throughout the examined scan-rate range. The capacitive-controlled term may include contributions from surface redox reactions, near-surface storage, and other kinetically rapid processes; therefore, it should not be assigned exclusively to surface adsorption. Similarly, the diffusion-influenced term does not by itself identify sulfate as the diffusing species. Therefore, the electrochemical response of layered MnO_2 is more appropriately described as a mixed kinetic process involving both capacitive-controlled and diffusion-influenced contributions. These kinetic results alone do not establish a sulfate-intercalation pseudocapacitance mechanism.

Elemental mapping provides complementary evidence for a state-dependent variation in sulfur-containing species during electrochemical polarization. As shown in Supplementary Figures 3 and 4, the S signal is broadly distributed over the Mn-containing electrode region after charging, indicating that sulfur-containing

species are not confined to a single isolated location at the spatial resolution of the energy-dispersive X-ray spectroscopy (EDS) measurement. At the charged state of 1.0 V *vs*. SCE, the normalized EDS contents of S and Mn are approximately 7.1 and 16.4 wt%, respectively. After discharge to 0 V *vs*. SCE, the corresponding normalized values are approximately 0.8 wt% for S and 25.0 wt% for Mn. Based on these semi-quantitative EDS values, the S/Mn atomic ratio is estimated to change from approximately 0.744:1 in the charged electrode to 0.055:1 after discharge. The pronounced decrease in the sulfur signal after discharge is consistent with the electrochemically associated uptake and subsequent removal of sulfur-containing species. Together with TGA and XPS/XAS results, the EDS analysis supports the involvement of sulfate-containing species in the electrochemical response of layered MnO_2.

First-principles calculations were further performed to evaluate the energetic feasibility of sulfate-anion migration within a model interlayer environment of layered MnO_2. As shown in Figure 3G, the calculated migration pathway of SO_4^{2-} in the MnO_2 interlayer region connects the selected initial and final interlayer configurations through a series of intermediate images. The energy profile reaches a maximum relative energy of approximately 0.22 eV along the calculated pathway. This relatively low barrier indicates that sulfate migration is not associated with a large energetic penalty within the adopted structural model. The optimized configurations further show that SO_4^{2-} can be accommodated within the modeled interlayer space without immediate collapse of the computational structure. These results support the energetic plausibility of interlayer sulfate accommodation and migration under the assumptions of the calculation. These theoretical results are compatible with the experimentally observed electrochemical response and the state-dependent variation in sulfur-containing species, although they do not establish a unique correspondence between the calculated pathway and the experimental mechanism.

Based on the above results, a sulfate-anion-involved charge-storage mechanism is proposed. During charging, oxidation of Mn species in the MnO_2 electrode is accompanied by an increased association of sulfate-containing species with the electrode. One plausible contribution is the partial accommodation of SO_4^{2-} within the accessible interlayer regions, together with possible surface or near-surface sulfate association. During discharge, the sulfur signal decreases and the Mn electronic state shifts toward its discharged-state characteristics, consistent with the partial removal of electrochemically associated sulfate-containing species. The combined experimental and computational evidence therefore supports sulfate-coupled charge compensation involving Mn-centered redox and mixed capacitive-controlled and diffusion-influenced kinetics. Possible interlayer accommodation may contribute to this process, but the present *ex situ* evidence does not unambiguously distinguish it from surface adsorption, near-surface storage, or electrolyte trapping. Compared with conventional metallic-cation-dominated storage mechanisms, sulfate-anion intercalation could provide an alternative charge-compensation pathway in structurally accessible host materials.

The device-level feasibility of this charge-storage chemistry was evaluated using aqueous MnO_2//MnO_2 symmetric cells, in which layered MnO_2 served as both the positive and negative electrodes. During charging, the two MnO_2 electrodes are driven toward different electrochemical states, requiring charge-compensation processes at both electrode-electrolyte interfaces. At the positively polarized electrode, Mn oxidation is accompanied by an increased association of sulfate-containing species with the electrode. Partial accommodation of SO_4^{2-} within accessible interlayer regions represents one possible charge-compensation pathway, although surface and near-surface sulfate association cannot be excluded. At the negatively polarized MnO_2 electrode, Mn reduction may be compensated by the uptake or redistribution of electrolyte cations, proton-related species, and/or interfacially adsorbed ions. During discharge, the electrode polarizations are reversed toward their initial states, accompanied by corresponding changes in Mn redox states and electrolyte-ion association. The schematic illustration of the discharge process and the associated

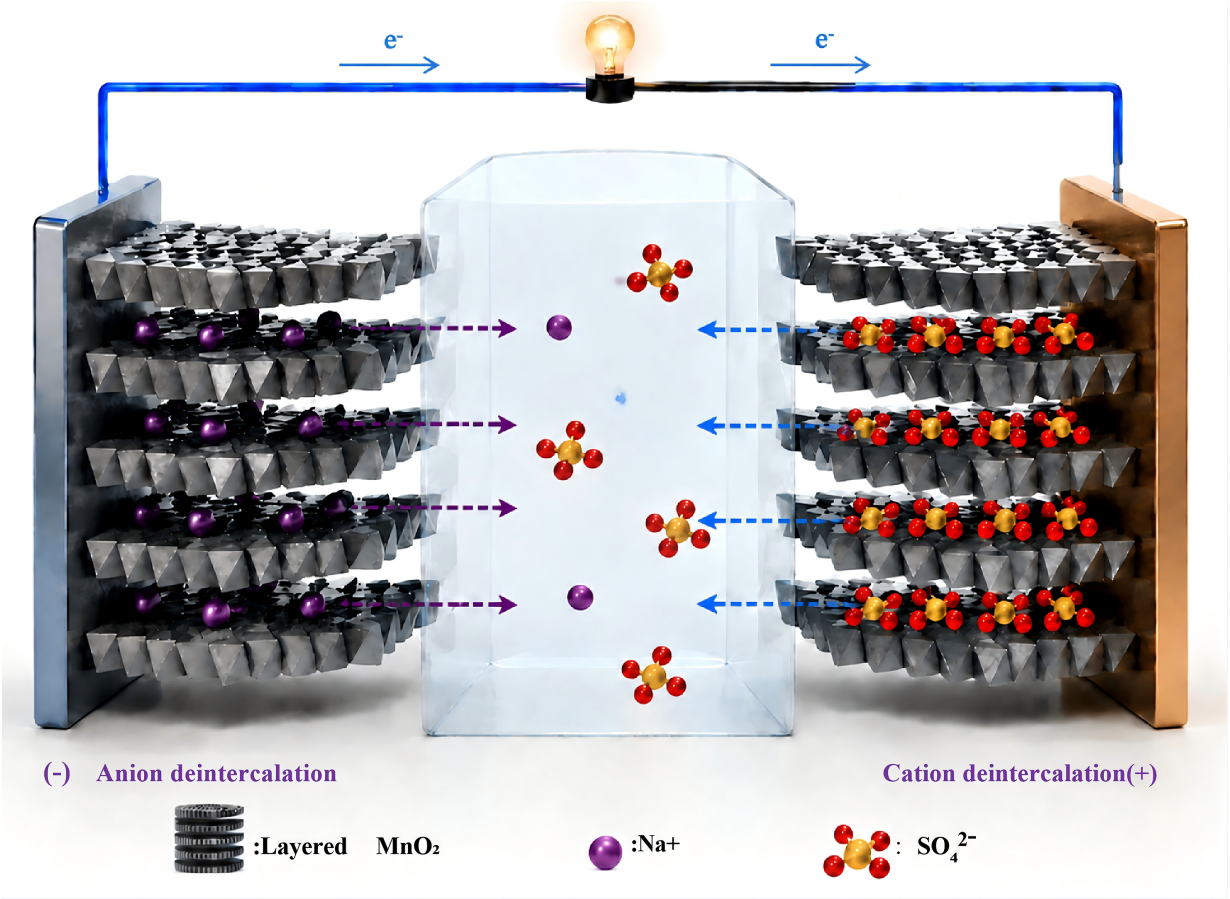

Figure 4. Conceptual schematic diagram of the MnO_2//MnO_2 symmetric cell.

ion redistribution behavior is shown in Figure 4. This symmetric configuration minimizes the influence of differences arising from dissimilar active materials and provides a platform for evaluating the compatibility of layered MnO_2 under both positive and negative polarization conditions.

The electrochemical performance of the MnO_2//MnO_2 symmetric cell is shown in Figure 5. To evaluate the polarity-dependent electrochemical response and accessible cell-voltage range of the MnO_2//MnO_2 symmetric configuration, CV measurements were performed in 0.5 M Na_2SO_4 electrolyte at a scan rate of 5 mV s^{-1} over different voltage ranges, as shown in Figure 5A. The voltage window was gradually expanded from −0.5 to +0.5 V, −0.7 to +0.7 V, −1.0 to +1.0 V, −1.4 to +1.4 V, −1.7 to +1.7 V, and finally −2.0 to +2.0 V. The CV curves display approximately mirror-symmetric responses about 0 V, showing that comparable electrochemical responses are obtained when the polarity of the nominally identical MnO_2 electrodes is reversed. The mirror-like response is consistent with the ability of either electrode to undergo positive or negative polarization in this configuration.

The charge-discharge curves in Figure 5B display nearly triangular profiles within a voltage window of 0-1.8 V, indicating a continuously varying cell voltage with a substantial capacitive-like contribution. The specific capacities calculated from the discharge curves are 119.8, 92.3, 76.6, 68.6, and 61.9 mAh g^{-1} at current densities of 0.2, 0.4, 0.6, 0.8, and 1.0 A g^{-1}, respectively, as shown in Figure 5C. All capacity and current-density values for the symmetric cell were normalized to the active mass of one MnO_2 electrode (the positive electrode during the GCD measurements). At 1.0 A g^{-1}, the cell retains approximately 51.7% of the capacity obtained at 0.2 A g^{-1} indicating that a substantial fraction of the low-rate capacity remains accessible under the examined higher-current condition.

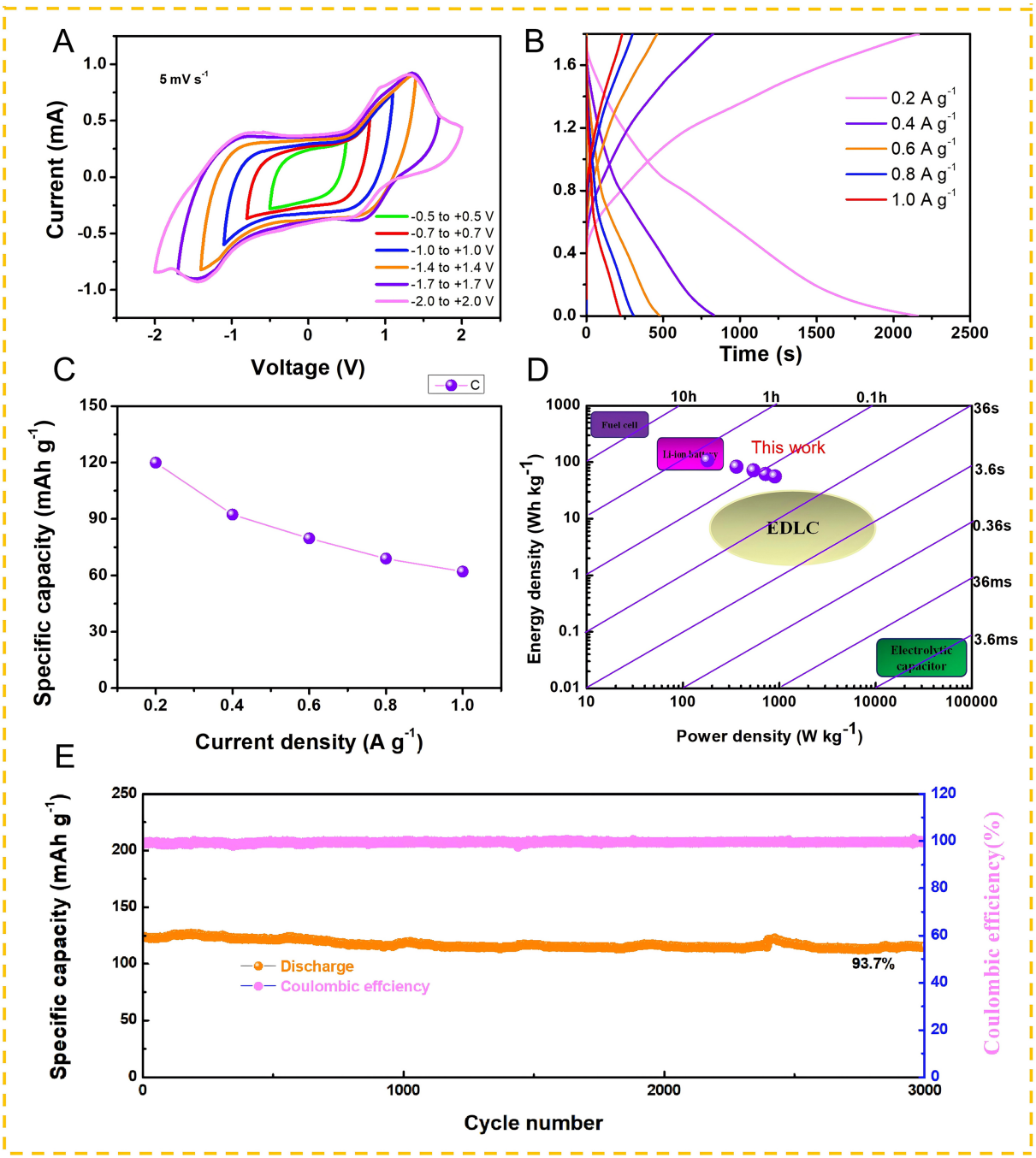

Figure 5. Electrochemical performance of the MnO_2//MnO_2 symmetric aqueous battery. (A) CV curves of the MnO_2//MnO_2 symmetric cell within different voltage windows. (B) GCD curves of the MnO_2//MnO_2 symmetric cell within a voltage window of 0-1.8 V. (C) Specific capacities at different current densities. (D) Ragone plot comparing the energy and power densities of the MnO_2//MnO_2 symmetric cell with previously reported energy-storage devices[45]. (E) Cycling performance of the symmetric cell in 0.5 M Na_2SO_4 electrolyte.

The Ragone plot in Figure 5D further illustrates the energy and power characteristics of the MnO_2//MnO_2 symmetric cell. The device delivers an energy density of 107.94 Wh kg^{-1} at a power density of 180 W kg^{-1}. Even when the power density increases to 900 W kg^{-1}, the energy density remains 55.8 Wh kg^{-1}. These values are consistent with the reported capacities and a nearly triangular discharge profile over 0-1.8 V[45]. These values indicate that the MnO_2 symmetric cell retains measurable energy output as the applied current is

increased. The enhanced performance may benefit from the layered morphology, electrochemically accessible Mn redox sites, and the combined capacitive-controlled and diffusion-influenced charge-storage response.

Long-term cycling stability was further evaluated, as shown in Figure 5E. The MnO_2//MnO_2 symmetric cell maintains 93.7% of its capacity after 3,000 cycles, with Coulombic efficiency remaining close to 100% after the initial activation period. The stable cycling performance indicates that the cell maintains a largely recoverable electrochemical response over the examined cycling period. The slight activation behavior during the early cycles may originate from gradual electrolyte penetration and progressive activation of electrochemically accessible sites. Overall, the high capacity retention and stable Coulombic efficiency support stable device operation and largely reversible overall charge transfer under the tested conditions.

These results collectively show that layered δ-MnO_2 can function under both positive and negative polarization in an aqueous nominally symmetric cell and that sulfate-containing species are involved in its electrochemical response. Structural characterization confirms the formation of layered MnO_2 with an expanded interlayer structure, while *ex situ* spectroscopic, thermal, and elemental analyses show state-dependent sulfur signals accompanied by Mn electronic-state evolution. Electrochemical measurements show high capacity, good rate capability, and long cycling stability. Therefore, sulfate-anion intercalation represents a plausible component of the proposed sulfate-coupled charge-compensation mechanism for aqueous MnO_2-based energy-storage devices. This approach may offer a promising direction for developing potentially low-cost, aqueous energy-storage systems.

CONCLUSION

In conclusion, layered MnO_2 was investigated as an electrode material for aqueous symmetric batteries, with sulfate-containing species examined as possible contributors to the charge-compensation process. Our results show state-dependent changes in sulfur-containing species accompanied by Mn-centered redox, while first-principles calculations indicate that interlayer SO_4^{2-} accommodation and migration are energetically plausible within the adopted structural model. Electrochemical kinetic analysis further reveals a mixed charge-storage response involving both capacitive-controlled and diffusion-influenced contributions. The MnO_2//MnO_2 cell delivers a specific capacity of 119.8 mAh g^{-1} at 0.2 A g^{-1} over a cell-voltage range of 0-1.8 V. A symmetric MnO_2//MnO_2 cell using 0.5 M Na_2SO_4 as the electrolyte achieves an energy density of 107.94 Wh kg^{-1} at a power density of 180 W kg^{-1} and maintains 55.8 Wh kg^{-1} at 900 W kg^{-1}. The cell also retains 93.7% of its reference capacity after 3,000 cycles, with the Coulombic efficiency remaining close to 100% after the initial activation period. The combined thermal, elemental, spectroscopic, electrochemical, and computational results support sulfate-coupled charge compensation in layered MnO_2. The results therefore expand the possible charge-compensation chemistry of aqueous MnO_2 electrodes beyond exclusively metal-cation-centered descriptions. The stable cell operation demonstrates the compatibility of layered MnO_2 with both positive and negative polarization under the investigated conditions. These findings highlight the potential of anion-involved charge compensation as a direction for broadening charge-carrier chemistry in aqueous manganese-based energy-storage systems.

DECLARATIONS

Authors' contributions

Conceptualization, methodology, investigation, writing - original draft: Tan, S.
Conceptualization, methodology: Liang, L.; Zhou, S.
Investigation, validation, resources: Meng, J.; Zhang, G.
Writing - review & editing: Bao, W.; Kyaw, A. K. K.; Liu, Q.
Supervision, conceptualization, funding acquisition, project administration, writing - review & editing: Yu, F.

Availability of data and materials

The data supporting the findings of this study are available within this Article and its Supplementary Materials. Further data are available from the corresponding authors upon request.

AI and AI-assisted tools statement

During the preparation of this manuscript, the AI tool DeepSeek (version 3, released on 2024-12-26) was used solely for language polishing. The AI-assisted tool Image 2 (gpt-image-2, released on 2026-04-21) was used for the preparation of Figure 4 and the Graphical Abstract. These tools did not influence the study design, data collection, analysis, interpretation, or scientific content of the work. All authors take full responsibility for the accuracy, integrity, and final content of the manuscript.

Financial support and sponsorship

This work was financially supported by the Natural Science Research of Jiangsu Higher Education Institutions of China (24KJB480012), the National Natural Science Foundation of China (52303234), the Natural Science Foundation of Guangdong Province (2024A1515010415, 2024A1515010773), and the Australian Research Council (DE240101231).

Conflicts of interest

All authors declared that there are no conflicts of interest.

Ethical approval and consent to participate

Not applicable.

Consent for publication

Not applicable.

Supplementary Materials

Supplementary Materials

REFERENCES

1. Abedi, P.; Farhadi, K.; Hosseini, S. A.; Hooshyari, K. Rational design of a superhydrophilic step-scheme MnO_2/NiCo-layered double hydroxide heterojunction anchored on anodized graphite substrate as a photoanode for boosted water splitting activity. *J. Environ. Chem. Eng.* **2026**, *14*, 120697. DOI
2. Dong, S.; Ren, H.; Yang, J.; et al. An aqueous proton battery under alkaline electrolyte. *Energy. Storage. Mater.* **2025**, *74*, 103888. DOI
3. Kulkarni, A.; Padwal, C.; Macleod, J.; Sonar, P.; Kim, T.; Dubal, D. Toward safe and reliable aqueous ammonium ion energy storage systems. *Adv. Energy. Mater.* **2024**, *14*, 2400702. DOI
4. Agustiana, D.; Daraz, U.; Siburian, D. M.; Lyu, P.; Liu, H. Cathode materials for advanced lithium-ion batteries: developments, challenges, and emerging trends. *Mater. Res. Bull.* **2026**, *195*, 113842. DOI
5. Plakia, L.; Kartsonakis, I. A. A review on design, synthesis and application of composite materials based on MnO_2 for energy storage. *Energies* **2025**, *18*, 3455. DOI
6. Hu, Y.; Li, H.; Gu, H.; et al. Anion redox-driven engineering of layered MnO_2 cathodes for high-capacity aqueous Al-ion batteries. *Chem. Eng. J.* **2025**, *524*, 168881. DOI
7. Hao, Y.; Yang, M.; Ma, H.; et al. Natural low corrosive phytic acid electrolytes enable green, ultrafast, stable and high-voltage aqueous proton battery. *Energy. Storage. Mater.* **2024**, *70*, 103455. DOI
8. Ran, Y.; Dong, F.; Sun, S.; Lei, Y. Aqueous zinc-based batteries: active materials, device design, and future perspectives. *Adv. Energy. Mater.* **2025**, *16*, 2406139. DOI
9. Liu, Y.; Meng, J.; Yue, M.; et al. Thermodynamically stable colloid dispersion electrolytes with the Tyndall effect for practical zinc-ion pouch cells. *Energy. Environ. Sci.* **2026**, *19*, 589-604. DOI
10. Poudel, M. B.; Anand, R.; Ojha, G. P.; et al. Nitrogen coordinated atomically dispersed manganese catalyzes oxygen reduction in practical zinc-air batteries and alkaline fuel cells. *J. Power. Sources.* **2026**, *678*, 239959. DOI

11. Poudel, M. B.; Kandel, D. R.; Lohani, P. C.; Kim, A. R.; Kwak, H. B.; Yoo, D. J. Enhanced electrochemical performance of dendritic Fe_2O_3 nanowires on hollow carbon nanofibers with manganese and phosphorus co-doping for solid-state symmetric supercapacitors. *J. Power. Sources.* **2026**, *661*, 238447. DOI
12. Bacirhonde, P. M.; Shrestha, D.; Kang, K.; et al. Understanding the metal-center mediated adsorption and redox mechanisms in a $FeMn(NbTa)_2O_6$ columbite material for anion exchange membrane water electrolyzers. *Adv. Energy. Mater.* **2025**, *15*, 2404479. DOI
13. Karim, O. L. A.; Poudel, M. B.; Bhandari, T.; Yoo, D. J. Integrating iron phthalocyanine and cobalt nanoparticles encapsulated N-doped CNTs as bifunction electrocatalyst for oxygen evolution reaction and oxygen reduction reaction in high-efficiency zinc-air battery. *J. Alloys. Compd.* **2026**, *1071*, 188725. DOI
14. Kannan, R.; Kim, A. R.; Nahm, K. S.; Yoo, D. J. One-pot synthesis and electrocatalytic performance of Pd/MnO_x/graphene nanocomposite for electrooxidation of ethylene glycol. *Int. J. Hydrogen. Energy.* **2015**, *40*, 11960-7. DOI
15. Shi, M.; Das, P.; Wu, Z. S.; Liu, T. G.; Zhang, X. Aqueous organic batteries using the proton as a charge carrier. *Adv. Mater.* **2023**, *35*, 2302199. DOI PubMed
16. Zhang, A.; Yin, X.; Zhang, X.; et al. 2D layered MnO_2 with an ultralarge interlayer spacing for aqueous zinc ion batteries. *ACS. Appl. Energy. Mater.* **2024**, *7*, 1298-305. DOI
17. Wang, J.; Wang, K.; Chen, C.; et al. Orbital-guided crystal phase engineering of MnO_2 via d-orbital-free alkali metal cation pillaring for high-stability supercapacitors. *J. Alloys. Compd.* **2025**, *1047*, 185145. DOI
18. Yang, H.; Zhang, T.; Chen, D.; et al. Protocol in evaluating capacity of Zn-Mn aqueous batteries: a clue of pH. *Adv. Mater.* **2023**, *35*, 2300053. DOI
19. Yang, S.; Wang, S.; Du, Y.; Sun, J.; Zhao, D.; Cao, B. Hydrogen bond engineering in aqueous electrolytes: strategies for cryogenic battery applications. *Energy. Storage. Mater.* **2025**, *82*, 104576. DOI
20. Wang, X.; Ye, J.; Yang, W.; et al. Bohr magnetons: microscopic disruptors of layered MnO_2 structures. *Adv. Funct. Mater.* **2025**, *35*, 2500650. DOI
21. Wang, L.; Zhang, B.; Zhou, W.; et al. Cation-in-mesopore complex for 20 Ah-level aqueous battery. *Angew. Chem. Int. Ed.* **2025**, *137*, e202501010. DOI
22. Zhao, J.; Tang, M.; Lan, H.; et al. An anode-free sodium dual-ion battery. *Energy. Storage. Mater.* **2024**, *70*, 103480. DOI
23. Zuo, Y.; Meng, T.; Tian, H.; et al. Enhanced H^+ storage of a MnO_2 cathode via a MnO_2 nanolayer interphase transformed from manganese phosphate. *ACS. Nano.* **2023**, *17*, 5600-8. DOI
24. Wang, S.; Guo, X.; Huang, K.; et al. Cooperative Jahn-Teller effect and engineered long-range strain in manganese oxide/graphene superlattice for aqueous zinc-ion batteries. *Nat. Commun.* **2025**, *16*, 5191. DOI PubMed PMC
25. Shi, H.; Chu, F.; Zhang, Y.; et al. Anode-less Li-based metal batteries and beyond: challenges, strategies, and prospects. *Mater. Today.* **2025**, *83*, 446-83. DOI
26. Qin, R.; Zhang, M.; Li, S.; Pan, F. Proton storage and transfer in aqueous batteries. *Matter* **2025**, *8*, 102165. DOI
27. Ruan, P.; Chen, X.; Qin, L.; et al. Achieving highly proton-resistant Zn-Pb anode through low hydrogen affinity and strong bonding for long-life electrolytic Zn//MnO_2 battery. *Adv. Mater.* **2023**, *35*, 2300577. DOI
28. Wang, F.; Lu, H.; Zhu, H.; et al. Mitigating the interfacial concentration gradient by negatively charged quantum dots toward dendrite-free Zn anodes. *Energy. Storage. Mater.* **2023**, *58*, 215-21. DOI
29. Yadav, P.; Kumari, N.; Rai, A. K. A review on solutions to overcome the structural transformation of manganese dioxide-based cathodes for aqueous rechargeable zinc ion batteries. *J. Power. Sources.* **2023**, *555*, 232385. DOI
30. Gao, X.; Wu, H.; Su, C.; et al. Recent advances in carbon-based nanomaterials for multivalent-ion hybrid capacitors: a review. *Energy. Environ. Sci.* **2023**, *16*, 1364-83. DOI
31. Li, G.; Sun, L.; Zhang, S.; et al. Developing cathode materials for aqueous zinc ion batteries: challenges and practical prospects. *Adv. Funct. Mater.* **2023**, *34*, 2301291. DOI
32. Li, L.; Wang, Y.; Meng, J.; et al. Boosting the capacitance of MOF-derived carbon-based supercapacitors by redox-active bromide ions. *Chem. Eng. J. Adv.* **2023**, *14*, 100484. DOI
33. Loh, J. R.; Xue, J.; Lee, W. S. V. Challenges and strategies in the development of zinc-ion batteries. *Small. Methods.* **2023**, *7*, 2300101. DOI PubMed
34. Yang, Y.; Qu, G.; Wei, H.; et al. Weakly solvating effect spawning reliable interfacial chemistry for aqueous Zn/Na hybrid batteries. *Adv. Energy. Mater.* **2023**, *13*, 2203729. DOI
35. Zhang, M.; Zhang, X.; Dong, Q.; et al. Organic molecular intercalated $V_3O_7{\cdot}H_2O$ with high operating voltage for long cycle life aqueous Zn-ion batteries. *Adv. Funct. Mater.* **2023**, *33*, 2213187. DOI
36. Zhang, R.; Feng, Y.; Ni, Y.; et al. Bifunctional interphase with target-distributed desolvation sites and directionally depositional ion flux for sustainable zinc anode. *Angew. Chem. Int. Ed.* **2023**, *62*, e202304503. DOI

37. Chen, J.; Zhao, W.; Jiang, J.; et al. Challenges and perspectives of hydrogen evolution-free aqueous Zn-ion batteries. *Energy. Storage. Mater.* **2023**, *59*, 102767. DOI
38. Li, L.; Wu, R.; Ma, H.; et al. Toward the high-performance lithium primary batteries by chemically modified fluorinate carbon with δ-MnO_2. *Small* **2023**, *19*, 2300762. DOI
39. Liang, G.; Mo, F.; Ji, X.; Zhi, C. Non-metallic charge carriers for aqueous batteries. *Nat. Rev. Mater.* **2020**, *6*, 109-23. DOI
40. Yao, H.; Yu, H.; Zheng, Y.; et al. Pre-intercalation of ammonium ions in layered *δ*-MnO_2 nanosheets for high-performance aqueous zinc-ion batteries. *Angew. Chem. Int. Ed.* **2023**, *62*, e202315257. DOI
41. Jin, Y.; Zou, L.; Liu, L.; et al. Joint charge storage for high-rate aqueous zinc-manganese dioxide batteries. *Adv. Mater.* **2019**, *31*, 1900567. DOI
42. Liu, L.; Wu, Y. C.; Huang, L.; et al. Alkali ions pre-intercalated layered MnO_2 nanosheet for zinc-ions storage. *Adv. Energy. Mater.* **2021**, *11*, 2101287. DOI
43. Wu, D.; Housel, L. M.; King, S. T.; et al. Simultaneous elucidation of solid and solution manganese environments via multiphase *operando* extended X-ray absorption fine structure spectroscopy in aqueous Zn/MnO_2 batteries. *J. Am. Chem. Soc.* **2022**, *144*, 23405-20. DOI
44. Dai, L.; Wang, Y.; Sun, L.; et al. Jahn-teller distortion induced Mn^{2+}-rich cathode enables optimal flexible aqueous high-voltage Zn-Mn batteries. *Adv. Sci.* **2021**, *8*, 2004995. DOI PubMed PMC
45. Yu, F.; Liu, Z.; Zhou, R.; Tan, D.; Wang, H.; Wang, F. Pseudocapacitance contribution in boron-doped graphite sheets for anion storage enables high-performance sodium-ion capacitors. *Mater. Horiz.* **2018**, *5*, 529-35. DOI